




Article

Carbon Aerogel-Supported Nickel and Iron for Gasification Gas Cleaning. Part I: Ammonia Adsorption

Oscar Gómez-Cápiro ^{1,2,*} , Adrian Hinkle ³, Aaron M. Delgado ¹, Camila Fernández ², Romel Jiménez ¹  and Luis E. Arteaga-Pérez ^{4,*} 

¹ Carbon and Catalysis Laboratory (CarboCat), Department of Chemical Engineering, Faculty of Engineering, University of Concepcion, Concepción 4100000, Chile; aaron.delgadom@icloud.com (A.M.D.); romeljimenez@udec.cl (R.J.)

² Technological Development Unit, University of Concepción, Concepción 4100000, Chile; c.fernandez@udt.cl

³ Department of Chemical Engineering, Oregon State University, Corvallis, OR 97331; USA; adrian.hinkle@gmail.com

⁴ Nanomaterials and Catalysts for Sustainable Processes (NanoCatpSP), Department of Wood Engineering, University of Bío-Bío, Concepción 4100000, Chile

* Correspondence: ogoomez@udec.cl (O.G.-C.); larteaga@ubiobio.cl (L.E.A.-P); Tel.: +56-952-209-754 (O.G.-C.)

Received: 19 July 2018; Accepted: 19 August 2018; Published: 25 August 2018



Abstract: Biomass gasification is a promising way to obtain “green energy”, but the gas composition makes it unsuitable for use in traditional technologies (i.e., IC engine). Gas purification over nickel and/or iron catalysts is an attractive alternative. Cellulose-based carbon aerogels (CAGs) have shown suitable physical chemical properties for use as catalyst supports. In this work, nickel and iron catalysts are supported on CAG made from cellulose microfibers. Microfibers were impregnated with $(\text{NH}_4)_2\text{SO}_4$ to increase the mass yield. Carbonization was evaluated at different heating rates, maximum temperatures, and dwell times to generate CAGs. Resulting chars were characterized by N_2 adsorption, X-ray diffraction (XRD), and Raman spectroscopy. The CAG with better properties (specific surface, pore size, thermal resistance) was impregnated with the metal precursor salt via incipient wetness and treated with H_2 . Catalysts were characterized by transmission electron microscopy (TEM), XRD, N_2 adsorption, and inductively coupled plasma optical emission spectrometry (ICP-OES). Ammonia adsorption was studied over CAG and catalysts to estimate the thermodynamic parameters. The impregnation with $((\text{NH}_4)_2\text{SO}_4$ improves thermal resistance of the char obtained from carbonization. The catalysts exhibit higher adsorption capacity than CAG (without metal), indicating chemical interaction between ammonia and metals. The metal-ammonia interaction is stronger on Fe than on Ni catalyst, which is consistent with reported theoretical calculations.

Keywords: cellulose nanofibers; carbon aerogel; nickel catalyst; iron catalyst; ammonia adsorption

1. Introduction

Biomass is an abundant and easy to harvest resource, but faces difficulties associated with distribution logistics (collection, transportation, and distribution). Furthermore, biomass, especially wood, has lower energy density ($2\text{--}3 \text{ GJ/m}^3$) than other common fuels such as ethanol (23 GJ/m^3) and gasoline (35 GJ/m^3) [1,2]. One of the most traditional and promising technologies for converting solid biomass into energy, fuels and commodities is gasification [3], but obtaining the desired products can be challenging. The composition of gasification gases (CO_2 , H_2 , CO , CH_4) can vary depending on gasifying agent (i.e., steam, air, oxygen), gasification temperature, reactors design, as well as feedstock composition. For example, Molino et al. [4] have reported that Pine sawdust gasification result in

a syngas composition with high content of CO (35–43%) and H₂ (21–39%), while CH₄ (6–10%) and CO₂ (18–20%) appear in lower concentrations. However, changing biomass type by α -cellulose the balance is quite different with less CO (6.5–11.2%), H₂ (13.5–18.5%), and CH₄ (2.2–3.7%) and increasing CO₂ (26.3–27.7%). Regardless of the gasification conditions, the syngas is contaminated with traces of undesirable species such as ammonia (NH₃) and sulphur compounds (H₂S, SO_x), with condensable polyaromatics known as tar and with solid particles [5]. These contaminants are not allowed for most technologies used downstream of the gasifier such as IC engine, turbines, FT-synthesis reactors, etc. Tar elimination is the higher investment and operations cost in gasification; thus, the removal of tar is a major means to reduce the overall cost of biomass gasification [5]. However, ammonia, even at low concentrations, is inadmissible for F-T synthesis processes and may limit the use of combustion gases due to the generation of NO_x [6]. Physical cleaning pathways eliminate these compounds by means of filters, water traps, rotary separators, electrostatic precipitators, etc. [7]. All of these technologies miss the potential energy present in the contaminants (especially tar) [8] and transfer the contaminants to another effluent (liquid or solid), which also requires treatment before disposition, thus elevating the operation costs [9]. A promising way to eliminate tar and ammonia is via thermal or catalytic cracking/reforming, which could also contribute to increase the concentration of CO_x and/or H₂ in the syngas [10–12]. Thermal cracking depends on temperature and begins to be effective over 1000 °C, so it requires special equipment, which elevates the installation costs [11]. Above this temperature, each 100 °C increase implies a caloric power loss of 3.5% [10]. Wet and dry reforming processes do not require high temperatures but depending on gasification conditions they could require an auxiliary service to supply steam or CO₂, respectively. Furthermore, both technologies require catalysts to reduce the activation energies of specific reactions [8,13–15]. Catalytic cracking works at the same temperature as reforming, but without the need of an auxiliary service, making it the most economically attractive technology. Oxides of alkaline and alkaline-earth metals, dolomites, and olivine have been reported as active for cleaning gasification gases, nevertheless, all of them are deactivated by agglomeration, coke deposition, and/or sintering at the reaction conditions [8,16]. According to [17,18], nickel is the most effective catalyst for catalytic upgrading of gasification gases. It has high activity for tar cracking, with high selectivity to H₂, and it is also capable of decomposing ammonia [19,20]. Iron is also used in this kind of reaction because it is considered the metal with highest activity for breaking carbon-carbon bonds [21]. It is also active for ammonia decomposition [22], and it is more abundant and environmentally manageable than nickel [23]. One of the main drawbacks of using metal catalysts to clean gasification gases is the coke formation, which is influenced by the operational conditions, and the catalyst and support properties [8].

The most used supports (e.g., alumina) act as reaction promoters, but they have a strong interaction with hydrocarbons so they are affected by coke formation, mostly on acid sites [24]. On the other hand, carbonaceous materials have proven to have a high affinity and adsorption selectivity to hydrocarbon compounds [25] such as tar. Apart from an easily tailorable porous structure and surface chemistry, carbon presents other advantages as a catalyst support: metals at the surface can be easily reduced; the structure is resistant to acids and bases and is stable at high temperatures if a proper treatment is used; the active phase can be easily recovered; conventional carbon supports usually have lower costs than other conventional supports, such as silica [26,27]; and higher resistance to surface coke formation [24]. Nevertheless, carbon supports also present some disadvantages, such as their low reproducibility, since different carbonization batches of the same raw material can contain varying ash amounts.

In particular, carbon aerogels (CAG) solve the problem of reproducibility because they are obtained from standardized raw materials, mostly by carbonization of cellulose microfibrils (MFCs) [28] or aerogels obtained via organic synthesis [29]. CAGs can be synthesized using a sol-gel process, generating an organic gel that is dried via freeze drying. The dry gel is pyrolyzed (carbonized) to obtain the corresponding CAG. Cellulose-based organic gels are of particular interest, as cellulose has high carbon content and it is renewable, chemically stable, and globally abundant [30]. Alternative synthesis methods, using different raw materials, include: sol-gel systems based on the crosslinking

of cellulose acetate with polyfunctional isocyanate in acetone [31]; sol-gel polymerization of linear phenolic resin and hexamethylenetetramine in alcoholic solutions [32]; sol-gel polymerization reaction of resorcinol and formaldehyde in water [33]. All of them correspond to organic synthesis with hazardous substances, which make more attractive the use of cellulose-based raw materials. Regardless of the synthesis method, CAGs present several advantages as catalyst supports, compared to common carbon materials. They allow a uniform distribution of metal particles at the surface, and the metal dispersion is stable upon heating treatments [34]; because of their nanostructure, they show higher thermal resistance [35] and mechanical strength [36]. In addition to catalyst supports, CAGs can be used as adsorbents, electrodes, and supercapacitors for secondary batteries, hydrogen storage, and desalination [37–39].

Morphological and structural properties of CAGs from cellulose can be easily manipulated by controlling the carbonization process (Table 1). According to Jazaeri et al., temperature and heating rate are key parameters in the carbonization [30]. Their experiments indicated that long holding times (above 17 h) and slow heating rates (below 2 °C/min) help to preserve desired fibrous morphology and acceptable mass yield, although reported mass yields are far from the theoretical 44.4 % of carbon in cellulose (about 15% [40]). Different strategies have been reported to increase mass yield: Impregnation of raw material with ammonium salts [41], carbonization under acid atmosphere (HCl) to promote a fast dehydration and avoid carbon losses [42], and modification of the carbonization conditions [43,44]. In particular, the impregnation with ammonium salts (i.e., ammonium sulphate) modifies the pyrolysis mechanism that is normally observed for biomass. It favours dehydration at lower temperatures and stabilizes the carbonaceous structure [45], which results in a lower mass loss.

Usually, higher carbonization temperatures lead to carbons with higher specific surface area, up to the point (different for each raw material) where the structure collapses as a result of the cross-linking of carbon atoms, which reduces the space between them [46]. Nevertheless, Table 1 shows that for CAGs, the temperature has a lower effect on the carbon surface area when lower heating rates and shorter dwell times are used, probably because the energy-to-time ratio is not enough to remove high amounts of solid mass to create more space between atoms and, consequently, higher porosity.

Table 1. Effect of temperature, dwell time, and heating rate on carbonized cellulose-based precursors reported in literature.

Researcher	Conditions			Results	
	T (°C)	Dwell Time (h)	Heating Rate r (°C/min)	S _{BET} (m ² /g)	r _{pore} (nm)
Brunner [44]	460	-	70	5.2–370 ^a	-
			0.03	610	-
	900	-	11	525	-
			70	470	-
Meng [28]	700	0.25	5	550	>4
	950			100	~5
Yu [47]	950	2	5	742	-
Xie [48]	400	8	2.5	2.6	45.5
	500			5.2	46
	700			438	45
	1000			449	44
Grzyb [49]	1000	1	4	117	4.5–7
	1100			165	4–7.5

^a first value: N₂ atmosphere carbonization, second value: CO₂ atmosphere carbonization.

Several authors have reported the use of CAGs as catalyst supports for the conversion of organic compounds that can be classified as tar. Maldonado-Hódar used CAGs-supported Pt catalysts to study the adsorption and decomposition of toluene, xylene and acetone, finding that even at high temperatures, the support retains part of these compounds [50]. Ábrahám et al. published a study about the acetic acid hydroconversion reaction over Mo/CAGs catalysts; their results show that the

reaction pathways and product distributions are controlled by the accessibility of carbon surface, as well as by the amount and shape of Mo particles [51]. Hai Woong Park et al. published an extensive work on lignin model decomposition over Pd/CAGs catalysts, showing the need of modifying the catalyst surface in order to reach the required performances [52,53]. These researches show that CAGs, used as catalysts support, have direct influence on activity and selectivity in tar decomposition reactions.

The use of carbon-supported catalysts for ammonia decomposition is not common. Research has mostly focused on ammonia adsorption over carbon and carbon-supported metals as a solution to emission control. Rodrigues et al. studied the influence of initial ammonia concentration and carbon bed temperature during the ammonia adsorption on activated carbon [54]. They found a direct dependence of adsorption capacity of ammonia over carbon with the amount of ammonia in fluid phase, contrary to rise temperature dependence. Bandosz and Petit used carbon from different sources and different metal impregnation to evaluate strength and amount of ammonia adsorbed over carbons surface and its interaction with metals particles [55]; they concluded that in unmodified carbon, porosity controls the adsorption process. More detailed studies on metal-ammonia interaction have been published using theoretical ways, in which the effect of support is not considered. Results suggest that the adsorption of ammonia on transition metal atoms, like Fe and Ni, occurs in bridge, hollow, and top positions, through the unpaired electrons in nitrogen [56–58]. Their results suggest a chemical interaction between ammonia and metals supported by calculated thermodynamics parameters.

CAG-based catalysts can be prepared using organics and inorganics precursors. Smirnova et al. impregnated CAG with Co-mesotetramethoxy-phenylporphine in tetrahydrofuran [59] and Hu et al. impregnated mesoporous CAG with $\text{Cu}(\text{NO}_3)_2 \cdot 3\text{H}_2\text{O}$ [38]. Most synthesis methods entail the addition of the active metal to the support via incipient wetness impregnation [33,60], followed by drying for 4 to 12 h, and calcination [61] and/or reduction for up to 7 h, at temperatures of maximum 400 to 600 °C, with slow heating rates.

In general, experimental studies show enhancement of adsorption capacity with carbon surface modification and metal impregnation independent of catalysis preparation methods. Thermodynamic parameters are defined by theoretical studies. Experimental data of thermodynamics parameters of ammonia adsorption over metallic phases over carbon are not determined.

In the present work, the adsorption of ammonia on over nickel and iron catalysts supported on cellulose-based CAG is studied, as a first step to propose a kinetic mechanism of gasification gas cleaning reactions. An experimental design was made for the synthesis of supports and catalysts used in the study of ammonia and tar decomposition reactions, the present report shows the first part related to support preparation and ammonia adsorption. The support (CAG) was produced from freeze-dried MFCs, which were carbonized at different carbonization temperatures (900, 1000, and 1100 °C), heating rates (10 and 20 °C/min), and dwell times (0, 1, and 2 h). As the support will be used for gasification gases catalytic upgrading, the lowest carbonization temperature was restricted at 900 °C, to guarantee the stability of support during operation, typically between 700 °C and 900 °C [62]. An impregnation of MFCs with ammonium sulphate was carried out to enhance the thermal resistance and mass yield of char in carbonization processes. Catalysts were characterized by X-ray diffraction (XRD), transmission electron microscopy (TEM) and inductively coupled plasma optical emission spectrometry (ICP-OES). Finally, the effect of temperature and initial ammonia concentration on the adsorption of ammonia over synthesized catalysts was studied.

2. Results and Discussion

2.1. Characterization of as-Prepared and pre-Treated Cellulose Microfibers

2.1.1. As-Prepared MFCs Composition

The elemental and ICP-OES analyses of as-prepared MFCs are shown in Table 2. The molecular formula estimated with the mass composition was quite similar to the pure cellulose (experimental: $\text{C}_{5.6}\text{H}_{10.6}\text{O}_{5.3}\text{N}_{0.04}$; theoretical: $\text{C}_6\text{H}_{10}\text{O}_5$). It is well known that alkaline and alkaline earth metals

have significant influence, as catalysts or precursors, in carbonization processes [63]. However, the low content of inorganics detected in MFCs by ICP-OES allows discarding their effect on the carbonization process.

Table 2. Cellulose microfiber (MFC) compositional analysis.

		Ultimate ^a (wt.%)				
		C	H	N	O ^b	
		41.2	6.52	0.21	52.07	
		Sugars ^c				
MFC	Glucose (%)	Xylose (%)		Extractive (%)		
	81.9	14.2		3.9		
		Inorganics				
	Ash (%)	Na (mg/g)	Ca (mg/g)	Fe (mg/g)	Mg (mg/g)	K (mg/g)
	<0.01	0.77	0.912	0.112	0.273	0.651
						Si (mg/g)
						0.005

^a Standard deviations (r) = %C ± 0.15, %H ± 0.008, %N ± 0.04, %Ash ± 0.008. ^b Oxygen was calculated by difference from C, H, N. ^c According to NREL/TP-510-42618.

2.1.2. Crystalline Structure

The crystalline structure of raw as-prepared and (NH₄)₂SO₄-treated MFCs were studied by X-ray diffraction. No significant differences were observed between both XRD patterns (Figure 1), with the main reflections appearing at the same 2θ positions.

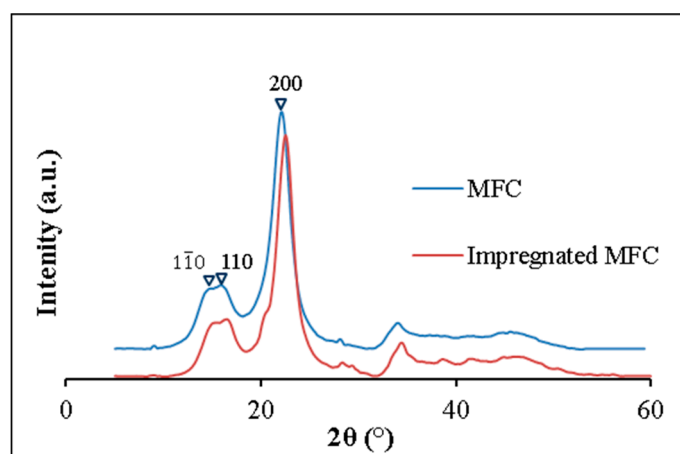


Figure 1. Normalized X-ray diffraction (XRD) patterns of cellulose microfiber (MFC) and pre-treated impregnated MFC.

Similar crystal parameters were calculated from the XRD analysis (Table 3) of as-prepared and pre-treated MFC materials, which also match the results reported for other celluloses [64]. Peaks positions can be assigned to the presence of (100), (010), and (110) crystallographic planes, for cellulose I α , and (1 $\bar{1}$ 0), (110), and (200) planes, for cellulose I β [65]. Negative Z-values, -27 and -72 for as-prepared and pre-treated MFC, respectively, indicate that both celluloses are predominantly of type I β , with a monoclinic structure. Accordingly, the signals appearing at 2θ of about 14.8° , 16.5° , and 22.2° are assigned to (1 $\bar{1}$ 0), (110), and (200) planes.

As show in Table 3, crystallite sizes change after treatment with ammonium salt, probably caused by partial dissolution of crystallites during impregnation. The CrI values calculated using Herman's equation (Equation (1b)) were slightly lower than the values of Segal's index. This result supports the well-known fact that Segal's index tends to overestimate the crystallinity. Based on results reported by Kim et al. [66], suggesting that cellulose with higher crystallite size has a higher thermal stability,

pre-treated MFC samples are expected to have a higher thermal stability that can also be expressed as a higher mass yield in the carbonization process.

Table 3. Crystalline index (Equation (1a,b)), d-spacing (Equation (3)), and crystal size (Equation (4)).

	Segal CrI (%)	Herman CrI (%)	d-Spacing (nm)			Crystallite Size (nm)		
			(110)	(110)	(002)	(110)	(110)	(002)
as-prepared MFC	79	74.2	0.6	0.544	0.395	3.6	2.7	3.9
pre-treated MFC	80.3	76.8	0.57	0.539	0.395	4.7	2.0	4.0

2.2. Carbon Aerogel Preparation

All MFC samples, as-prepared and pre-treated with an ammonium-based solution, were carbonized at different temperatures and times, under N₂ flow. Initially, nine CAG samples were prepared and three of them (those prepared without a dwell time after reaching the pyrolysis temperature) were selected for elemental analysis (Table 4).

Table 4. Elemental analysis of selected carbon aerogels (CAG 90, CAG 100, and CAG 110).

Sample	Carbon wt. %	Nitrogen wt. %	Hydrogen wt. %	Oxygen wt. % *	Sulphur wt. %	Ash wt. %
CAG 90	91.20	1.7	0.8	~5.3	BDL	<1
CAG 100	92.50	2.0	0.9	~3.6	BDL	<1
CAG 110	90.70	1.3	0.6	~6.4	BDL	<1

* calculated by difference.

In all the samples, the carbon content exceeds 90 wt.%, which is a characteristic feature of carbon aerogels (Standard 472:1999). Furthermore, the sulphur and nitrogen contents are very low, indicating that all S-species from the ammonium salt were removed during the drying and carbonization processes.

The textural properties of CAGs materials were correlated to the different carbonization conditions used in the synthesis, aiming to identify the conditions leading to CAG materials with the best properties as catalyst support for tar decomposition. Particularly, surface area and pore volume measured by N₂-physisorption were considered in the first screening. A full table with all the carbonization conditions and carbon material properties is provided in a Supplementary Material (see Table S1).

Results from N₂ physisorption analysis at 77 K are shown in Figure 2a,b. As observed, the specific surface area (S_{BET}) and pore volume decrease with the increase in temperature and dwell time. According to Marsh and Rodriguez-Reinoso [46], this behavior is common in carbonization. Depending on the carbon precursor, the specific surface area reaches a maximum at a certain temperature, due to the release of small molecules (i.e., water and methanol) allowing the free space that constitutes the porosity. Further increases of temperature cause loss of heteroatoms and cross-linking of carbon atoms, which reduces the space between them and essentially closes off porosity. For MFC as precursor material, results (shown below) indicate that the maximum specific surface area of carbon is reached at a temperature lower than 900 °C. An additional sample was prepared at 800 °C (CAG 80), while the other synthesis conditions were the same as for CAG 90. The textural characterization for this sample is included in Table 5; following the same trend, and in agreement with the results from Marsh and Rodriguez-Reinoso [46], the specific surface was even higher, although other textural properties did not significantly change, compared to the samples prepared at higher temperatures.

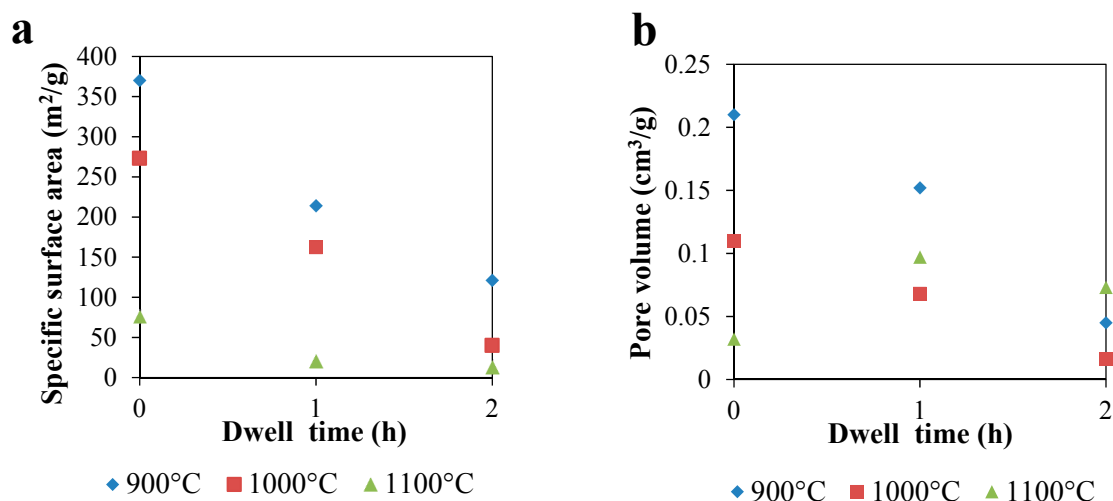


Figure 2. Effect of dwell time and temperature on morphology of carbon aerogels (CAGs). (a) Specific surface area, (b) pore volume. Heating rate: 10 °C/min.

Table 5. Comparison between pre-treated and pure MFC, carbonized at the same conditions.

CAG	Mass Yield	Specific Surface (m ² /g)	Pore Volume (cm ³ /g)	Pore Size (nm)
80	28.0	464	0.20	10.2
90	27.7	370	0.19	11.0
90-0%	13.9	327	0.17	10.2

Adsorption-desorption N₂ isotherms and pore size distribution of CAG 90 are shown in Figure 3. The isotherms can be classified as type IV, according to IUPAC classification. This shape is associated with mesoporosity and condensation inside the pores [67]. Mesoporosity is an advantageous characteristic for catalyst supports used in the decomposition of aromatic compounds, since the kinetic diameter of typical tar molecules is in the range 6.9–10.7 Å [68].

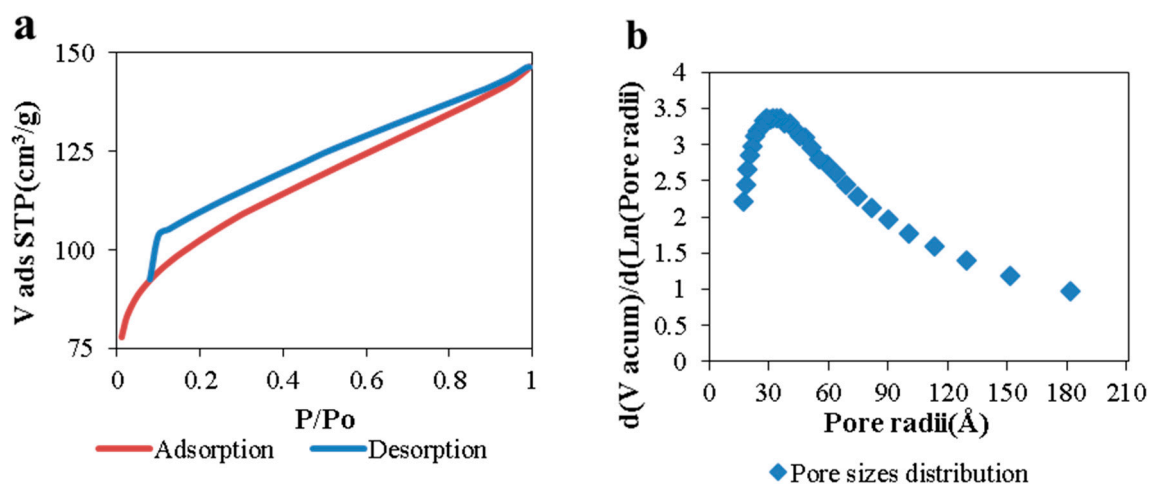


Figure 3. N₂ adsorption-desorption isotherms at 77 K (a) and pore size distribution (b) for CAG 90.

Another key parameter in CAG production via MFC carbonization is the mass yield, defined as the quantity of carbon remaining in the CAG times that contained in the MFCs. Several authors argue that the low carbon yields of cellulose-derived CAGs are a restriction for the process economy. MFCs used

in this work were pre-treated with ammonia-based salts, which has been reported as an alternative to increase the carbon yield [45]. Regardless of the carbonization temperature or time, the mass yield of all materials, pre-treated with 5 wt.% $(\text{NH}_4)_2\text{SO}_4$, ranged from 26 to 28%. For the carbonization of as-prepared MFC, without any treatment, the yield is reduced to almost the half (CAG 90–0%, Table 5). These values are in line with those reported by Kulenkampff [40] and Arteaga et al. [69]. When the heating ramp used in carbonization is increased to 20 °C/min, the increase in mass yield achieved by sulphate impregnation is 23–69% lower. This behaviour matches with findings previously reported, showing that higher heating rates cause greater mass losses, as observed in Table 1. Besides its effect on yield, the impregnation with $(\text{NH}_4)_2\text{SO}_4$ has no major effects on the textural properties of CAGs.

Thermogravimetric analysis was used to compare the thermal resistance of CAG samples (Figure 4a). Note that CAG 110 has its maximum mass loss at a lower temperature than CAG 90, however, the mass loss rate (%/min) is lower than CAG 90 at the same conditions. Starting from 350 °C until the temperature of maximum mass loss, DTG increases almost linearly with the temperature, with a “slope” (rate of mass loss per °C). Plots can be compared by this “slope” or by the temperature at which the maximum mass loss rate occurs (Figure 4b). In any case, CAG 90–0% has the lowest thermal resistance, confirming that ammonium sulphate pre-treatment has a positive effect on this property. For CAGs prepared from pre-treated MFC, the thermal resistance increases with the carbonization temperature, CAG 110 > CAG 90 > CAG 80. Activated carbon Pittsburgh has the highest resistance among all samples, probably due to an activation process carried out at high temperatures and for long times, resulting in a thermally stable structure.

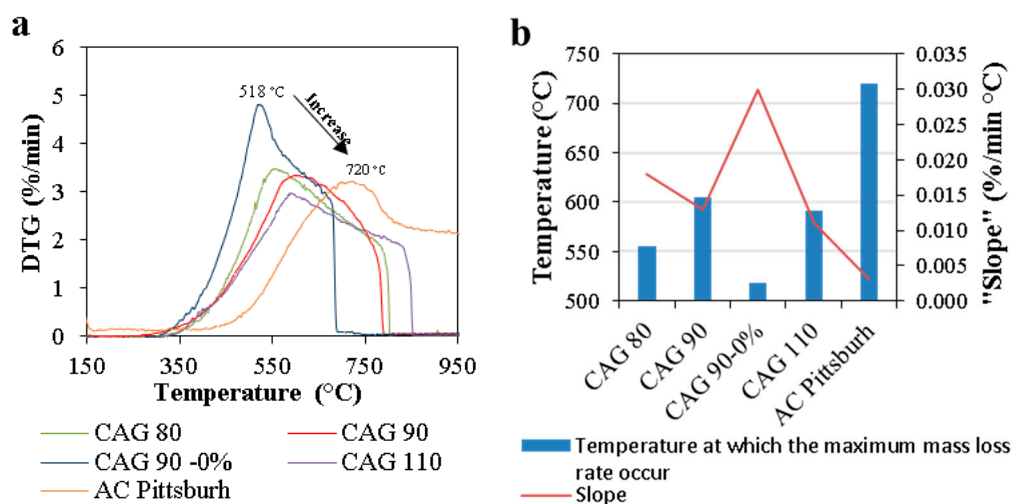


Figure 4. DTG for thermal resistance in air with heating rate: 10 °C/min; air flow: 80 mL/min (a). Comparison between thermal resistance indicators in chars' samples (b).

To complement the thermal resistance results, CAGs and activated carbon were analyzed by XRD and Raman spectroscopy, respectively. The results from those analyses were also used to study the crystallite and chemical structure of all the materials.

Main reflections in the XRD patterns of the CAGs (Figure 5) agree with those reported in literature for other cellulose-derived chars [30]. None of the CAGs prepared here reach graphitization, which occurs above 2000 °C and leads to a singular reflection at $2\theta = 26.5^\circ$ [46,70]. In contrast, all CAG samples showed two wide reflections, at 23.4° and 44.4° , assigned to the (002) and (010) planes of the amorphous carbon structure. Both peaks are characteristic of disordered chars, and have been reported in earlier investigations published by Biscoe et al. [71]. All CAGs patterns show a shoulder at around 15° , which is more pronounced for CAG 80, having almost the same intensity as the signal assigned to the (002) carbon plane. This specific signal could be related to the $(1\bar{1}0)$ and/or (110) planes of cellulose remaining after carbonization.

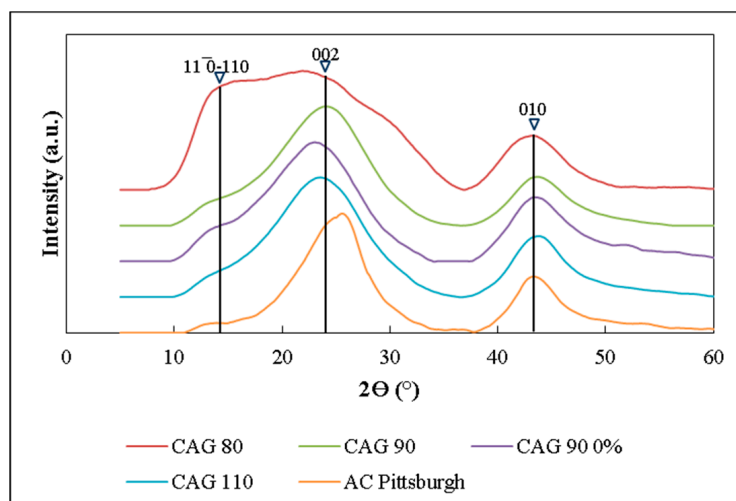


Figure 5. Normalized XRD pattern for CAG 80, 90, 90 0%, 110, and commercial activated carbon Pittsburgh.

Raman spectra of the synthesized CAG materials are shown in Figure 6. In the analysis of ordered carbonaceous materials like graphite, D and G bands usually refer to Defect and Graphite structures, respectively. However, X-ray diffraction (XRD) spectra of CAGs did not show any characteristic signal of graphitization ($2\theta = 26.5^\circ$), so D and G bands do not belong to defects and graphite structures, respectively [72]. D band might represent C–C bonds between aromatic rings and aromatics with no less than 6 rings. On the other hand, G bands can be attributed to the aromatic ring breathing rather than the E_{2g}^{2g} fundamental vibration of graphite. The band at 2700 cm^{-1} is a result of the second order phonon related to the disorder in the stacking of carbon layers [73]. Heavy aromatic compounds confer higher thermal resistance to any char. Assuming that bands areas are proportional to the concentration of their associated compounds, a higher ratio between D (1300 cm^{-1}) and G (1590 cm^{-1}) areas can be interpreted as a higher thermal resistance. In the same way, Lc (from (002) plane) and La (from (010) plane) crystallite dimensions (Ec. 4) have a direct proportionality with thermal resistance. As expected, the highest values of La, Lc and AD/AC ratio (shown in Table 6) were obtained for the commercial activated carbon Pittsburgh, since it has the highest thermal resistance. This fact helps to confirm that the higher ordered carbons are prone to have a higher thermal resistance, which is in line with the effect of ammonium salt on the carbonization mechanism, as shown in a previous work [69]. However, only La value follows the same relative order of CAGs materials as in terms of thermal resistance. Lc and AD/AG values for CAG 80 are out of trend, which could be associated to a different structure or the presence of some non-carbonized fractions of cellulose (in agreement with the signal at 15° detected in XRD patterns).

Table 6. Graphite crystallite dimensions (from X-ray diffraction (XRD) analysis) and bands D and G areas ratio (from Raman spectroscopy analysis).

Sample	Dimensions (nm)		AD/AG
	Lc	La	
CAG 80	0.67	3.36	1.73
CAG 90	1.03	3.17	3.05
CAG 90 0	1.02	2.90	2.92
CAG 110	0.97	3.27	2.99
AC Pittsburgh	1.28	3.78	3.23

Based on the above discussion on the textural properties, elemental analysis, and thermal resistance of the CAG materials, the CAG 90 sample, prepared by carbonization of $(\text{NH}_4)_2\text{SO}_4$ -treated MFCs at 900 °C and 0 h holding time, was selected as the material gathering the best properties as catalyst support for gasification gas cleaning applications. Therefore, the ammonia absorption study presented in the upcoming sections was performed using CAG 90-supported catalysts.

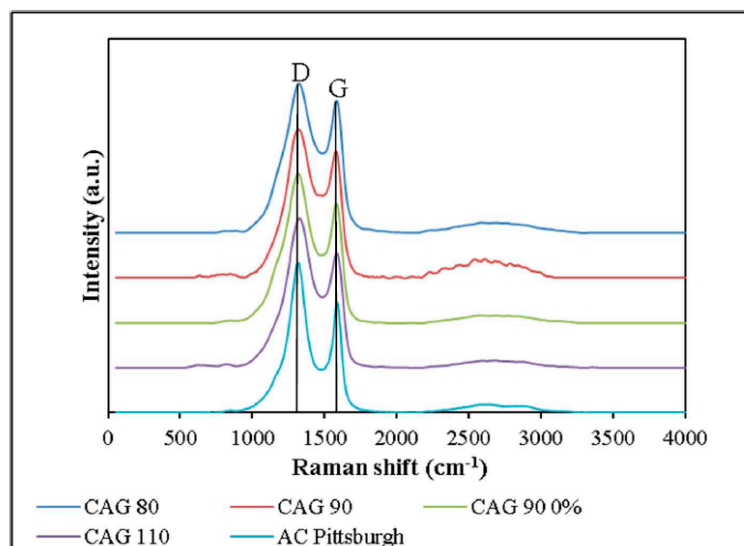


Figure 6. Normalized Raman spectra for CAG 80, 90, 90 0%, 110, and commercial activated carbon Pittsburgh.

2.3. Catalyst Synthesis and Characterization

2.3.1. Superficial and Composition Characteristics

Synthesized catalysts have been denoted as Ni/CAG 90 and Fe/CAG 90. Specific surface area (S_{BET}) of catalysts are 306 m^2/g and 288 m^2/g for Ni/CAG 90 and Fe/CAG 90, respectively, close to 17–22% lower than the area of the corresponding support (370 m^2/g), presumably due to pore blockage during metal impregnation [60]. The metal loading calculated by theoretical mass balance (10 wt.%), agreed to that measured by ICP-OES analysis: 9.8 wt.% of Ni in Ni/CAG 90, and 9.4 wt.% Fe in Fe/CAG 90. This metal content was used along with the particle size distribution to estimate the surface metal dispersion.

2.3.2. XRD Patterns. Catalysts

XRD patterns for both catalysts are shown in Figure 7. Nickel catalyst exhibited two reflections at $2\theta = 44.4^\circ$ and 51.7° , which are characteristic of (111) and (200) planes of metallic nickel with a face centered cubic structure (fcc) [60]. In the case of Fe catalyst, peaks at 44.6° , 65° , and 82.2° are characteristic of metallic iron and correspond to (110), (220), and (211) planes, respectively [74]. The absence of peaks at 30° , 35.6° , and 38.5° , corresponding to FeO, Fe_2O_3 , and Fe_3O_4 [75], suggests that iron oxides were not formed or were fully removed in the reduction treatment. Weak reflections around $2\theta = 23^\circ$ are assigned to the amorphous phase of CAG 90 support.

Sizes of metal crystallites were calculated from Scherrer's equation for both catalysts, and the results are presented in Table 7. Since particle sizes are usually overestimated by XRD analysis, the sizes were verified by transmission electronic microscopy (TEM).

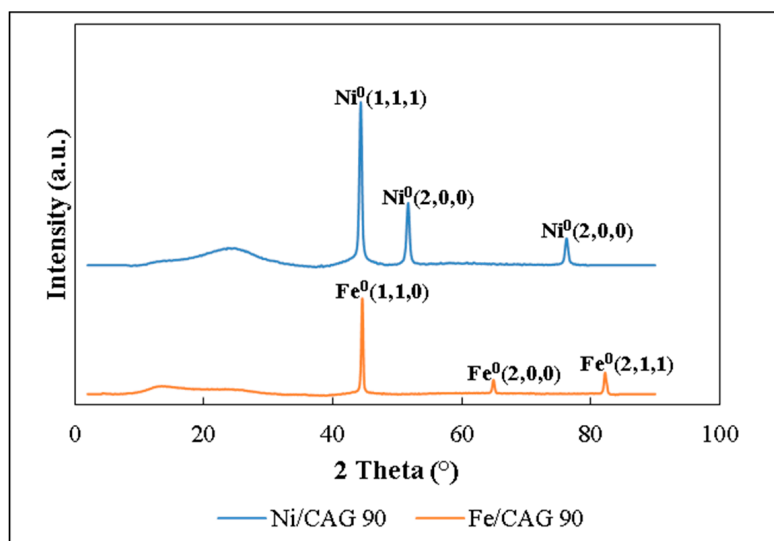


Figure 7. XRD patterns of Ni/CAG 90 and Fe/CAG 90 catalysts.

Table 7. XRD crystallite size (Equation (1)) for selected Ni and Fe crystal planes in both catalysts.

Catalyst	Crystallite Size (nm) XRD			Crystallite Size (nm) TEM
	(111)	(200)	(110)	
Ni/CAG 90	9.6	15.9	-	28.9
Fe/CAG 90	-	-	14.3	24.7

2.3.3. TEM

Transmission electron microscopy was used to obtain the size distribution of metal particles in both catalysts. Figure 8 shows a TEM image for each catalyst, while Figure 9 presents the frequency histograms of particle sizes, obtained from the measurement of more than 300 particles on each catalyst. These distributions together with the metal content were used to estimate the exposed metal surface in each catalyst. Spherical shape of particles is characteristic of the predominant metallic phase, as was shown in the XRD patterns. The average size of metal particles is shown in Table 7.

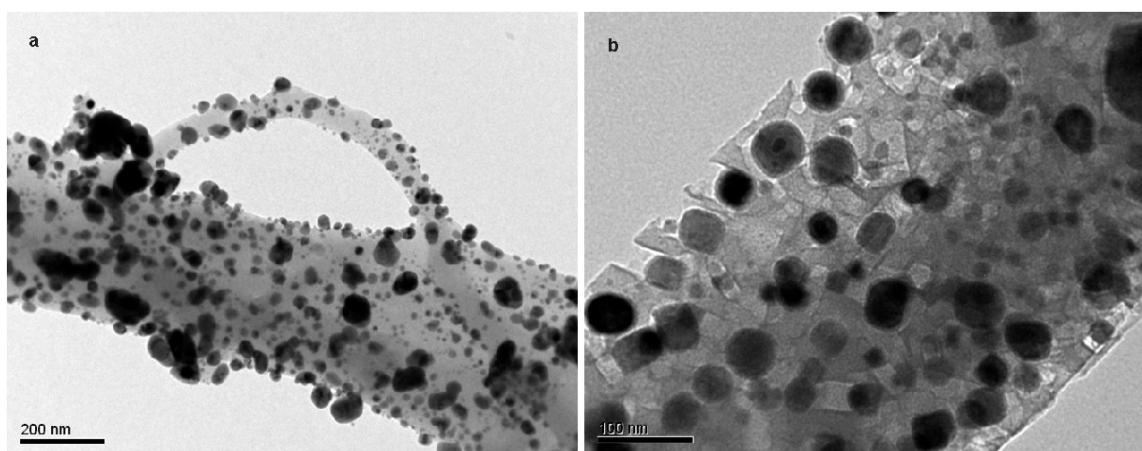


Figure 8. TEM of Ni/CAG 90 (a) and Fe/CAG 90 (b).

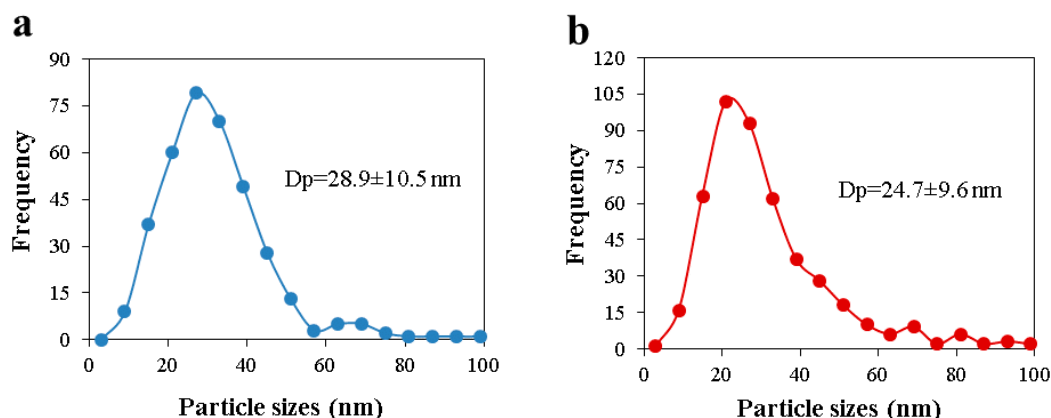


Figure 9. Particle size distribution for Fe/CAG 90 (a) and Ni/CAG 90 (b).

2.4. Adsorption Experiments

2.4.1. Ammonia Adsorption over CAG 90

Quantities of ammonia adsorbed on CAG 90 are shown in Table 8, as milligrams of NH_3 per gram of adsorbent, taking as a reference the quantity adsorbed ($2.13 \text{ mg NH}_3/\text{g CAG}$) at the conditions selected as saturation (0°C and 494 ppm) once reached equilibrium. For an inlet concentration of 390 ppm , the quantity of ammonia adsorbed ranges from 0.19 to $0.45 \text{ mg NH}_3/\text{g CAG 90}$, for temperatures in the range 50 – 150°C . Similar results on adsorbed quantities have been already reported. Zheng et al. [76] reported 1 mg of NH_3 adsorbed per gram of char, at 23°C and an inlet ammonia concentration of 500 ppm . Rodrigues et al. [54] worked at an inlet ammonia concentration of 600 ppm and reported 0.63 , 0.31 , and $0.22 \text{ mg NH}_3/\text{g char}$, at 40 , 80 , and 120°C , respectively. NH_3 can be adsorbed on (and interact with) the surface through various mechanisms, roughly categorized into: Non-specific van der Waals force, dissolution in water film adsorbed on the surface, and Brønsted acid-base interactions (mainly carboxylic acid sites via ammonium ions) [76]. Char surface can be modified to enhance its adsorption capacity, thus promoting ammonia adsorption mechanisms, but this is not the aim of the present work. No water was supplied to the system and the presence of oxygenated groups in alpha positions was discarded by Raman spectroscopy analysis, where the signal at 1700 cm^{-1} , assigned to $\text{C}=\text{O}$ groups [77], was not found. Consequently, non-specific van der Waals forces are expected to prevail in ammonia adsorption on CAG 90 surface.

Table 8. Ammonia adsorbed over CAG 90 ($\text{mg NH}_3/\text{g CAG 90}$).

Ammonia Relative Pressure	$\text{mg NH}_3/\text{g CAG 90}$		
	50°C	100°C	150°C
0.000135	$0.22 \pm 1.84 \times 10^{-3}$	$0.07 \pm 3.84 \times 10^{-4}$	$0.02 \pm 4.47 \times 10^{-5}$
0.000193	$0.35 \pm 1.29 \times 10^{-3}$	$0.15 \pm 1.61 \times 10^{-4}$	$0.06 \pm 5.89 \times 10^{-6}$
0.000232	$0.39 \pm 1.14 \times 10^{-3}$	$0.22 \pm 1.09 \times 10^{-3}$	$0.04 \pm 1.62 \times 10^{-4}$
0.000332	$0.41 \pm 3.09 \times 10^{-3}$	$0.19 \pm 1.77 \times 10^{-3}$	$0.10 \pm 7.24 \times 10^{-4}$
0.000390	$0.45 \pm 6.77 \times 10^{-4}$	$0.28 \pm 8.25 \times 10^{-5}$	$0.19 \pm 6.54 \times 10^{-4}$

Figure 10 shows the resulting isotherms at 50 , 100 , and 150°C . Langmuir and Freundlich, models do not perfectly represent the adsorption behavior. Freundlich's model overestimates NH_3 coverage at low pressures, but it is a good fit for higher coverages. On the contrary, Langmuir model better fits low ammonia coverages. High temperatures exhibit highest errors, which is in line with that already reported by Saha and Deng [78] for the study of ammonia adsorption over alumina. Models and thermodynamic parameters shown in Tables 9 and 10, respectively, were regressed using adsorption

data. The values obtained for entropies and enthalpies using the Freundlich model are markedly higher than for Langmuir's, given that the former is better suited for the higher values of the quantity loaded, it was expected that the thermodynamic parameters were the highest between the two models. The Freundlich adjustment was worse than that obtained by the Langmuir model, which reflects the error associated with the thermodynamic parameters. In a recent paper, Rezaei et al. [79] reported similar values of adsorption enthalpy over metal oxide nanoparticles suggesting that NH_3 was physisorbed on metallic clusters.

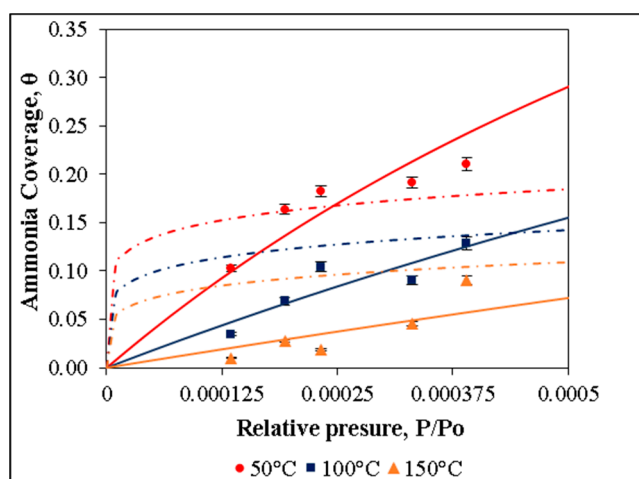


Figure 10. Coverage of ammonia over CAG 90 and model representation. Freundlich model presented by dashed lines and Langmuir model by solid lines.

Table 9. Langmuir and Freundlich models' parameters and statistical adjustment.

Temperature °C	Langmuir Model' Parameters		Freundlich Model' Parameters		
	K	R ²	Ko	Q _{ad}	R ²
50	909.09	0.75	3.2×10^{-5}	7516.9	0.92
100	322.58	0.81	0.56	2469.8	0.61
150	94.33	0.86	0.91	2169.9	0.59

Table 10. Thermodynamics parameters for ammonia adsorption over CAG 90.

Model	ΔH (kJ/mol)	ΔS (J/mol K)
Langmuir	-20.7 ± 0.509	-7.61 ± 0.43
Freundlich	-30.1 ± 3.9	-45.11 ± 7.7

Domingo-García et al. [80] reported adsorption enthalpies between -61.5 and -122 kJ/mol, for carbonaceous materials with chemical modification. On the other hand, Saha et al. [78] got similar values to this work for alumina without modification (-35.6 to -15 kJ/mol), where the adsorption mechanism was the interaction by non-specific van der Waals forces as it is postulated that happens in this case. It is worth noticing that, under real gasification conditions, the adsorption process could be affected by the presence of other species (e.g., CO_2 , CO , CH_4 , H_2 , and tars), which might change the above-reported values. In this regard Vasiliev et al. [81], studied the adsorption of CH_4 , H_2 , and NH_3 over activated carbon fibers and demonstrated that hydrogen is only adsorbed at cryogenic temperatures while the adsorption capacity for NH_3 was nearly twice that of CH_4 at 40°C . These results suggest that the affinity of carbon for NH_3 was higher than for the other gases; although the study did not include the simultaneous feed of those gases, which do not allow verifying if there is any

competition for adsorption sites. An extra issue that could involve working with gasification gas, is the presence of steam which could lead to an adsorption mechanism ruled by the dissolution in water film adsorbed on the surface. Nevertheless, this will happen if the carbon is used at temperatures below water dew point.

2.4.2. Ammonia Adsorption over Catalysts

Table 11 shows the quantity of ammonia adsorbed by both catalysts Ni/CAG 90 and Fe/CAG 90.

Table 11. Ammonia adsorbed over catalysts (mg NH₃/g catalyst).

Ammonia Relative Pressure	Temperature (°C)					
	50		100		150	
	Fe	Ni	Fe	Ni	Fe	Ni
0.000135	$0.46 \pm 4.63 \times 10^{-5}$	$0.38 \pm 2.24 \times 10^{-4}$	$0.26 \pm 1.33 \times 10^{-3}$	$0.21 \pm 5.12 \times 10^{-4}$	$0.08 \pm 3.90 \times 10^{-4}$	$0.16 \pm 1.56 \times 10^{-5}$
0.000193	$0.60 \pm 2.10 \times 10^{-3}$	$0.72 \pm 3.61 \times 10^{-4}$	$0.31 \pm 1.32 \times 10^{-3}$	$0.46 \pm 5.07 \times 10^{-3}$	$0.17 \pm 2.30 \times 10^{-4}$	$0.21 \pm 9.27 \times 10^{-4}$
0.000232	$0.74 \pm 6.56 \times 10^{-3}$	$0.73 \pm 2.72 \times 10^{-3}$	$0.54 \pm 4.33 \times 10^{-4}$	$0.51 \pm 1.60 \times 10^{-3}$	$0.19 \pm 9.59 \times 10^{-4}$	$0.26 \pm 1.43 \times 10^{-3}$

A positive effect of metal clusters on the adsorption process was observed by comparing the adsorbed quantities to those obtained with the support. Some studies suggest that N atoms bind to Ni surface, and H atoms are pointing outwards [82,83], probably due to the electronic configuration of Ni, which has two unpaired electrons in d orbital capable of accepting the 2 unshared electrons of N atoms. This could explain the enhancement of the adsorption capacity when Ni is added. Other authors [56,57] have used DFT methods to study ammonia adsorption over Fe surface. They have demonstrated that ammonia is preferentially adsorbed on on-top sites rather than bridge or hollow sites. The binding with iron surface occurs through the lone electron pair in N atom. On-top sites have electron deficiencies, which explains their strong interaction with the electron-rich N atoms [84]. Thus, adsorption over both metallic surfaces has the same geometry configuration with H atoms pointing outwards. However, the fact that Fe has four unpaired electrons—2 more than Ni—does not mean that it adsorbs more ammonia. Table 11 does not show a clear difference between adsorption capacity for both catalysts. Only when the values are normalized (see Figures 11 and 12) it is observed that, at same condition, Fe surface has less than 50% of ammonia coverage, while Ni is almost fully covered. This difference is given by the fact that Ni was able to adsorb less ammonia than Fe in reference conditions (0 °C and 490 ppm). The normalized value of ammonia adsorbed on the metal surface, calculated by subtracting what is adsorbed on the support and considering the available metal surface (estimated by Equation (11a)), showed that the Ni surface is able to adsorb 0.48 mg NH₃/g Ni, under reference conditions, while the amount admitted by Fe is more than double (1.05 mg NH₃/g Fe). Analyzing this from the point of view of the temperature, the adsorption capacity of Fe decreases more with the temperature than the adsorption capacity of Ni. Assuming that the adsorption capacity is conditioned by ammonia-metal interaction and this interaction depends on the ability of the metal atom to accept the unpaired electrons of N (as proposed by Lanzani et al. [84]), the Fe atoms/adsorbed ammonia stoichiometric ratio is higher than Ni atoms/adsorbed ammonia ratio. The increase in temperature will cause an increase in the movements of the atoms forming the ammonia molecule with respect to its center of mass and the molecule with respect to the surface. Therefore, the new equilibrium state will be affected in the case of Fe by the changes in surface-ammonia and ammonia-ammonia interactions. The influence of this last interaction will be less marked on the surface of Ni because the ammonia molecules are more distant each other. According with this supposition, ammonia adsorption enthalpy is more sensible to coverage changes over Fe surface than over Ni surface as observed in Figure 12.

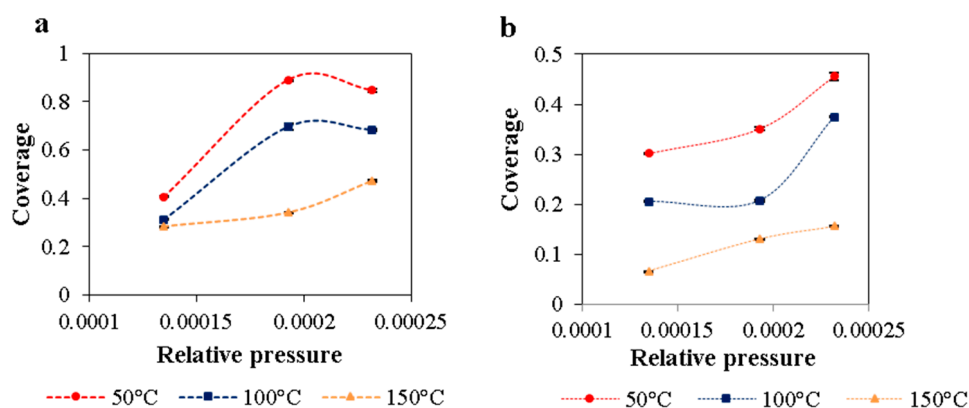


Figure 11. Ammonia Coverage over Ni surface (a) and over Fe surface (b).

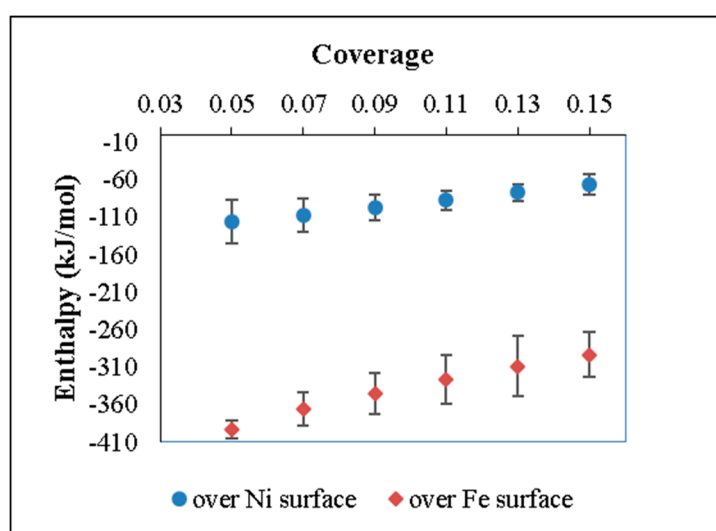


Figure 12. Variation of Enthalpy of ammonia adsorption with coverage of ammonia over metals surfaces.

Enthalpy values are in line with the theoretical estimations of Diawara [85], which reported a -84.5 kJ/mole ammonia adsorption enthalpy over Ni (111) surface with 12.5% of coverage. Calculated enthalpy for this coverage by interpolation with our experimental results has a value of -79.8 kJ/mol. The difference is probably due to a non-exclusively on-top adsorption as it was assumed in the theoretical work. Some ammonia molecules can be adsorbed on bridge or hollow sites energetically weaker than on-top sites. In the case of Fe, Otero et al. [57] show values of enthalpy of ammonia adsorption between -92.6 and -153.4 kJ/mole in nanoclusters with 16 and 190 Fe atoms respectively, all for 25% of coverage. The experimental determinations shown in Figure 12, exhibited an enthalpy of -191.3 kJ/mole for the same coverage, which is in the same order of magnitude. An important conclusion from Otero's calculations is that the adsorption energies increases with the size of the nanoclusters, which could be the cause for the slight differences in the enthalpy estimations.

3. Materials and Methods

3.1. Microfibers Treatment

The University of Maine (USA) provided the freeze-dried microfibers used for CAGs preparation. The MFCs were prepared from a gel produced from a Bleached Kraft Pulp at 3 wt.% of solids. The gels were freeze-dried according to the procedure reported by Demers [86] and known as ice segregation

induced self-assembling (ISISA). The MFCs were treated with a flame retardant, according to a procedure reported elsewhere [87]. The freeze-dried MFCs, previously ground, were conformed as disk-shape pellets in a Parr press (Parr Instrument Company, Moline, IL, USA). The pellets were impregnated via incipient wetness with an appropriate amount of ammonium sulphate ($(\text{NH}_4)_2\text{SO}_4$, 99.5 % purity, Merck) to get 5 wt.% (dry basis) of salt in the pellets. Impregnated samples were dried at 40 °C for 20 h, and the impregnation effectivity was confirmed by gravimetric analysis.

3.2. Carbon Aerogel Preparation. Carbonization

Carbonization was carried out in a split Thermo Scientific Lindberg/Blue M tube furnace. Approximately 7.4 g of pre-treated MFC pellets (36 pellets) were stacked in aluminium-oxide trays, which were placed parallel to the direction of a N_2 gas flow (Air Liquide, 99.999% purity, Coronel, Chile) of 20 mL/min/g of sample. The furnace was heated up to the selected temperature (900 °C, 1000 °C, or 1100 °C), at a constant heating rate of 10 °C/min and maintained at that temperature for different dwell times (0, 1, or 2 h). Resulting samples were denoted as CAG XY, where X is the number of hundreds of Celsius degrees at which the carbonization was carried out, and Y is the number of hours of dwell time. For example, the sample treated at 900 °C with a dwell time of 1h was denoted as “CAG 91”, and the sample treated at 1100 °C with 0 h of dwell time was denoted as “CAG 110”. An additional sample was prepared from the as-prepared MFC, at 900 °C and 0 h of dwell time, and it was denoted as “CAG 90–0%”.

3.3. Catalysts Preparation

Catalysts with a metal loading of 10 wt.% (nickel or iron) were prepared via incipient wetness impregnation. Nickel nitrate ($(\text{Ni}(\text{NO}_3)_2 \cdot 6\text{H}_2\text{O}$, >99% purity, Merck) and iron nitrate ($\text{Fe}(\text{NO}_3)_3 \cdot 9\text{H}_2\text{O}$, >99% purity, Merck) were used as metal precursors. The selected CAG support was ground with an agate mortar (<80 meshes). Afterwards, the corresponding nitrate aqueous solution was slowly added to the CAG support, in the appropriate quantities to reach 10 wt.% of metal in the final catalyst, according to the pore volume determined by N_2 adsorption-desorption (see Section 3.6). Nickel and iron loading samples were dried at 105 °C for 4 h, and ground again. Both solids were reduced for 2 h at 700 °C, under 40 mL/min of hydrogen, using a heating rate of 2 °C/min.

3.4. Compositional Analysis

Inductively coupled plasma optical emission spectrometry (ICP-OES) (Pekin-Elmer, Waltham, MA, USA) analysis was performed to determine the actual content of nickel and iron on the catalysts. MFC and CAG samples were also characterized using standard practice for elemental analysis [64] and a Leco True Spec analyzer (LECO Argentina S.A., Buenos Aires, Argentina). The main and trace inorganic elements were quantified by using a PerkinElmer Optima 7000 DV ICP-OES series instrument (Pekin-Elmer, Waltham, MA, USA).

3.5. N_2 Adsorption-Desorption at 77K

N_2 adsorption was performed to estimate the specific surface area, by Brunauer-Emmet-Teller (BET) model and pore volume. Barret-Joyner-Halenda (BJH) pore size distribution was determined using desorption data. Both isotherms were recorded in a Micromeritics Gemini VII 2390t device (Micromeritics, Communications Dr, Norcross, GA, USA), for MFCs, CAGs, and catalysts. Prior to tests, 0.2–0.5 g of samples were properly degasified, at 105 °C for MFC and 150 °C for other solids, under a continuous pure N_2 flow, during 24 h, as recommended by De Lange et al. [88].

3.6. Thermal Resistance

A Netzsch TGA thermobalance (model STA 409 PC) (Netzsch, Selb, Germany) was used to compare CAGs thermal resistances in oxidizing atmosphere. Samples (~20 mg) were heated from

room temperature up to 1000 °C, at 10 °C/min, under a constant air flow of 80 mL/min (Air Liquide, 99.999% purity, Coronel, Chile). Different CAG samples were analysed together a commercial activated carbon (Pittsburgh) used here like patron to compare characteristics. Furthermore, thermal resistance of the CAG selected for supporting Ni and Fe, was compared with another CAG sample prepared at the same conditions, but without treatment with ammonium sulphate.

3.7. X-ray Diffraction (XRD)

XRD analysis of as-prepared and (NH₄)₂SO₄-treated MFCs, CAGs, and catalysts were performed to evaluate the crystallinity, crystallite size, and polymorphy of the samples. The same commercial activated carbon (Pittsburgh) was analyzed as a reference to compare with the CAGs. The XRD patterns were recorded in a Bruker AXS model D4 Endeavor diffractometer (Bruker AXS GmgH, Karlsruhe, Germany), using monochromatic CuK α radiation ($\lambda = 0.15418$). The signal was generated at 40 kV and 20 mA. The intensities were measured in the range $5^\circ < 2\theta < 60^\circ$ for MFCs, and $5^\circ < 2\theta < 90^\circ$ for CAGs and the catalysts, with a step size of 0.02° and scans at 1 s/step. The crystalline index for MFC was determined by the well-known empirical method proposed by Segal [89] (Equation (1a)) and further corrected by the Herman's equation (Equation (1b)).

$$\text{CrI} = (I_{200} - I_{\text{am}})/I_{200} \quad (1a)$$

$$\text{CrI} = A_{\text{Cryst}}/A_{\text{Total}} \quad (1b)$$

where I_{200} and I_{am} are the intensities in plane (200) and amorphous phase, respectively, A_{Cryst} is the total area of crystalline bands, and A_{Total} is the total area of the XRD pattern.

The Z-function of [90] (Equation (2)) was used to determine the crystal structure ($I\alpha$ or $I\beta$) based on d-spacing. This discriminant analysis states that for $Z < 0$, the most probable structure is monoclinic ($I\beta$), and on the contrary, if $Z > 0$, triclinic ($I\alpha$) structure prevails.

$$Z = 1693 \times d_1 - 902 \times d_2 - 549 \quad (2)$$

where d_1 is the d-spacing of plane ($\bar{1}\bar{1}0$) and d_2 is the d-spacing of the (110) peak, and they are determined according to Bragg's correlation:

$$n \times \lambda = 2 \times d \times \sin(\theta) \quad (3)$$

where n is the order of reflection, d the interplanar spacing, and θ is the angle of incidence. $Z > 0$ indicate cellulose type $I\alpha$ (triclinic crystallite structure) and $Z < 0$ indicate cellulose type $I\beta$ (monoclinic crystallite structure).

The crystallite apparent size was calculated using the Scherrer's equation for all solids (Equation (4)).

$$L = (K \times \lambda)/(\beta \times \cos(\theta)) \quad (4)$$

where K is a constant equal to 0.94 for all cellulose and catalyst samples. For char, K is equal to 1.84 in (010) plane and 0.89 in (002) plane to calculate the graphitic crystallite dimensions L_a and L_c [68], λ is wavelength (in nm), β is the full width at half maximum intensity (FWHM) (in rad), and θ is the plane angle.

3.8. Raman Spectroscopy Analysis

Raman spectra was obtained in a LabRAM HR Evolution Raman spectrometer (HORIBA Scientific) (Horiba Ltd., Kyoto, Japan) with excitation laser wavelength of 633 nm, in a range of 50–4000 cm^{-1} . The obtained spectra were decomposed according to the peak/band assignment proposed by X. Li et al. [72], using OriginPro 8 software (OriginLab, Northampton, MA, USA). Raman spectra reveal CAGs surface chemical structure, specially oxygenated groups; its presence in alpha position increases

the adsorption capacity of chars due to acid-base interactions with ammonia [91]. To compare all Raman spectra, a ratio between D (1300 cm^{-1}) and G (1590 cm^{-1}) bands area was used, in this case a higher ratio is associated with better thermal stability because D bands is associate with graphite, more thermally stable than G bands associate with disordered carbon [92]. It is expected the absence of graphitization in the CAGs. Activated carbon Pittsburgh was analyzed using Raman spectroscopy to compare with CAGs, just like in thermal resistance and XRD analyses.

3.9. Transmission Electron Microscopy (TEM)

The metal cluster sizes for both catalysts were observed by transmission electron microscopy in a JEOL JEM 1200 EXII device (JEOL Ltd., Peabody, MA, USA), with voltage 120 kV. Each sample was suspended in a solution of ethanol-water (50–50 wt.%), supported in a copper grill and covered by a carbon layer. The size distribution and mean cluster sizes for each catalyst were estimated after measuring more than 300 metal particles in 10 images.

3.10. Ammonia Adsorption Experiment

Ammonia adsorption was studied over a selected support and both catalysts at 50, 100, and 150 °C, using N₂ as carrier gas. The total flow was kept unchanged to guarantee the same residence time in all experiments. The adsorption tests were carried out in a system consisting of a furnace (Omega Eng, CRFC-312/240-C-A, Stamford, CT, USA), into which a U-quartz reactor was placed with 0.4 g of CAG or catalyst (particle size $\leq 53.3\ \mu\text{m}$). Mass flow controllers (Aalborg series GFC, WReichman, Chile) were used to control the ammonia (Air Liquide, at 1000 ppm, N₂ balance) and N₂ (Air Liquide, 99.999% purity, Coronel, Chile) flows to achieve the required ammonia concentration, i.e., 135, 193, 232, 331, and 390 ppm for CAG support and 135, 193, 232 ppm for CAG-supported Ni and Fe catalysts. An electrochemical-type detector (Dräger X-am 7000, Drägerwerk AG & Co. KGaA, Lübeck, Germany) was used to measure ammonia concentration in the gas phase. The detector was calibrated before each measurement, as suggested [55,93]. Prior to each experiment, the CAGs samples were in situ degassed for 4 h at 150 °C in N₂ flow. Catalysts samples were heated up to 400 °C using a heating rate of 2 °C/min, under constant H₂ flow (Air Liquide, 99.999% purity, Coronel, Chile). This treatment was performed to eliminate adsorbed water and oxide formed over the catalyst surface during the manipulation of reduced samples. Furthermore, this was done to avoid the presence of adsorbed oxygen that can modified the interaction metal-ammonia drastically [83]. Each temperature-ammonia concentration point corresponds to a certain quantity of ammonia adsorbed, which was calculated by integration of breakthrough curve, just as reported in literature for similar ammonia adsorption studies [54,91,94]. In this work, the experiments were stopped after reaching the equilibrium and the breakthrough curves were numerically integrated. The calculated quantity was normalized per gram of solid. To determine the quantity of ammonia adsorbed on the metal surface, the corresponding quantity adsorbed on CAG was estimated from the metals/CAG specific surface ratio as it is explained later.

The data was treated with Langmuir (Equation (5)) and Freundlich (Equation (6a)) models to obtain equilibrium constant. Thermodynamic parameters were calculated with equilibrium constant using van't Hoff linearized equation (Equation (7)). Freundlich model was taken as proposed by Vannice [95].

$$\theta = K \times P_r / (1 + K \times P_r) \quad (5)$$

where θ is the coverage, K is the equilibrium constant, and P_r is the relative pressure assuming ideal gas behavior.

$$\theta = (K_o \times P_r)^{R \times T / Q_{ad}} \quad (6a)$$

where θ is the coverage, K_o is defined by Vannice [95] in Equation (6a), R is the universal gas constant (J/mol K), T is the temperature (K), and Q_{ad} is the heat of adsorption (J/mol).

$$K_o = e^{(\Delta S^\circ / R)} \quad (6b)$$

where ΔS° is the entropy (J/mol K) change associated to the adsorption process in standard conditions.

$$\ln K = \ln (\Delta S_{\text{ads}})/R + (\Delta H_{\text{ads}})/(R \times T) \quad (7)$$

where ΔS_{ads} (J/mol K) is the entropy change for adsorption process, and ΔH_{ads} (J/mol) is the enthalpy change associated to adsorption process.

A total surface coverage was required to model the adsorption data obtained for each sample (CAG selected as support, supported nickel and iron). In this work, coverage obtained from adsorption experiments performed at 0 °C and 490 ppm of ammonia were considered as reference for total coverage. These experiments were carried out following the same procedure described before but placing the U-quartz reactor inside an ice bath. Defined as θ , coverage was calculated as follows:

$$\theta = (\text{NH}_3 \text{ ads. at } T_i; P_{ri})/(\text{NH}_3 \text{ ads. at } T = 0 \text{ }^\circ\text{C}; P_r = 0.000490 \text{ ppm}) \quad (8)$$

where T_i and P_{ri} are the temperature and the relative pressure in experimental condition "i".

The metal surface for each catalyst was calculated by considering the particle size distribution obtained from TEM images. Both distributions (Fe/CAG and Ni/CAG) were extrapolated to reach one gram of pure metal at surface, using Solver tool. The objective function (Equation (9)) included a volume calculated from density (at room temperature) of each metal. The restriction (Equation (10)) was kept constant the ratio between particles counts for each particle size range of the distribution by selecting one range as a reference. The surface area (Equation (11a)) was estimated assuming that particles were hemispheres with the plane of the circumference in contact with the support. Thus, each metal particle has only the convex area of the hemisphere exposed.

$$\sum_i^n V_i = V_r \quad (9)$$

where V_i is the volume for each metallic particle and V_r is the volume of a gram of pure metal (Ni or Fe).

$$N_i/N_j = \text{constant} \quad (10)$$

where N_i is a quantity of particles established in the counts made from TEM images in a specific size range "i" and N_j is a quantity of particles established in the counts made from TEM images in the reference range j.

$$A_t = \sum_i^n A_i \quad (11a)$$

where A_t is the exposed surface per gram of metal according with previous assuming and A_i is defined by:

$$A_i = 2 \times \pi \times r^2 \quad (11b)$$

The final result is a metallic surface exposed value per gram of metal; the latter was calculated according to real metal content obtained by ICP-OES.

4. Conclusions

Carbonization conditions were studied for MFCs samples impregnated with ammonium sulphate. After characterization, CAG 90 was chosen as the catalyst support due to high superficial area without any activations and thermal resistance, along with its light preparation conditions compared to the other chars. In general, the study of preparations conditions for char show no dependence between mass yield and temperature with a heating rate of 10 °C/min. Thermal resistance comparison between a CAG prepared at identical conditions to CAG-90 but without ammonium sulphate impregnation shows a positive effect of salt pre-treatment in final CAGs structure, evidenced in higher temperature of maximum mass lost for carbonized pre-treated samples. Ammonium impregnated MFC samples reach twice the mass yield of untreated samples after carbonization; once impregnated, changes in

carbonization conditions practically did not cause changes in this yield. The decrease in performance results in a greater volume of pores and specific surface area, but no change in pore size was noted. Textural properties for CAGs resulting from pre-treated MFCs change with carbonization conditions, decreasing specific surface and pore volume as the temperature increased; pore size average did not vary significantly. Preparation conditions of both catalysts over CAG-90 yielded poor dispersion values. However, ammonium adsorption capacity for catalysts are higher than CAG 90 due to electronic interaction between d orbitals in both metals atoms and unshared electrons in N atom of ammonia molecule. Comparison between metals show higher ammonia adsorption capacity for Fe than Ni, furthermore, ammonia adsorption enthalpy over Fe surface is more sensible to coverage change than over Ni surface. For CAG 90, the Langmuir and Freundlich models were adjusted to isotherms, adsorbed amounts and thermodynamics parameters were in accordance with literature reports for char without surface modifications after carbonization, assuming CAG-ammonia interactions of the van der Waals type. Estimated enthalpy variation for ammonia adsorption over metal surfaces are near to previous reports in theoretical study.

Supplementary Materials: The following are available online at <http://www.mdpi.com/2073-4344/8/9/347/s1>. Table S1. MFC carbonization experimental conditions and CAGs textural properties.

Author Contributions: O.G.-C., R.J. and L.E.A.-P. conceived and designed the experiments; O.G.-C., A.H. and A.M.D. performed the experiments; O.G.-C. and A.H. analyzed the data; C.F. contributed with data analysis, grammar; O.G.-C. wrote the paper.

Acknowledgments: The authors would like to thank FONDECYT project 11150148, BMBF project 20150029, CONICYT PIA/APOYO CTE AFB170007 of the Technological Development Unit of the Universidad de Concepción, Chile. CONICYT-PFCHA/National PhD./2016-21160609. Also, to Douglas Bousfield of the University of Maine for providing us with MFC and for his unconditional support.

Conflicts of Interest: The authors declare no conflict of interest.

References

1. Tumuluru, J.S.; Sokhansanj, S.; Hess, J.R.; Wright, C.T.; Boardman, R.D. REVIEW: A review on biomass torrefaction process and product properties for energy applications. *Ind. Biotechnol.* **2011**, *7*, 384–401. [[CrossRef](#)]
2. Wakeley, H.L.; Griffin, W.M.; Hendrickson, C.; Matthews, H.S. Alternative Transportation Fuels: Distribution Infrastructure for Hydrogen and Ethanol in Iowa. *J. Infrastruct. Syst.* **2008**, *14*, 262–271. [[CrossRef](#)]
3. Vamvuka, D.; Karouki, E.; Sfakiotakis, S.; Salatino, P. Gasification of Waste Biomass Chars by Carbon Dioxide via Thermogravimetry—Effect of Catalysts. *Combust. Sci. Technol.* **2012**, *184*, 64–77. [[CrossRef](#)]
4. Molino, A.; Larocca, V.; Chianese, S.; Musmarra, D. Biofuels production by biomass gasification: A review. *Energies* **2018**, *11*, 811. [[CrossRef](#)]
5. Dong, L.; Asadullah, M.; Zhang, S.; Wang, X.S.; Wu, H.; Li, C.Z. An advanced biomass gasification technology with integrated catalytic hot gas cleaning Part I. Technology and initial experimental results in a lab-scale facility. *Fuel* **2013**, *108*, 409–416. [[CrossRef](#)]
6. Min, Z.; Lin, J.Y.; Yimsiri, P.; Asadullah, M.; Li, C.Z. Catalytic reforming of tar during gasification. Part V. Decomposition of NO_x precursors on the char-supported iron catalyst. *Fuel* **2014**, *116*, 19–24. [[CrossRef](#)]
7. Zwart, R.W.R. *Gas Cleaning Downstream Biomass Gasification Status Report*; ECN: Petten, The Netherlands, 2009.
8. Min, Z.; Asadullah, M.; Yimsiri, P.; Zhang, S.; Wu, H.; Li, C.Z. Catalytic reforming of tar during gasification. Part I. Steam reforming of biomass tar using ilmenite as a catalyst. *Fuel* **2011**, *90*, 1847–1854. [[CrossRef](#)]
9. Brandin, J.; Tunér, M.; Odenbrand, I. *Small Scale Gasification: Gas Engine CHP for Biofuels*; Linnaeus University: Växjö, Sweden, 2011.
10. Asadullah, M. Biomass gasification gas cleaning for downstream applications: A comparative critical review. *Renew. Sustain. Energy Rev.* **2014**, *40*, 118–132. [[CrossRef](#)]
11. Huber, G.W.; Iborra, S.; Corma, A. Synthesis of transportation fuels from biomass: Chemistry, catalysts, and engineering. *Chem. Rev.* **2006**, *106*, 4044–4098. [[CrossRef](#)] [[PubMed](#)]
12. El-rub, Z.A.; Bramer, E.A.; Brem, G. Review of Catalysts for Tar Elimination in Biomass Gasification. *Ind. Eng. Chem. Res.* **2004**, *43*, 6911–6919. [[CrossRef](#)]

13. Sutton, D.; Parle, S.M.; Ross, J.R.H. The CO₂ reforming of the hydrocarbons present in a model gas stream over selected catalysts. *Fuel Process. Technol.* **2002**, *75*, 45–53. [[CrossRef](#)]
14. Li, D.; Tamura, M.; Nakagawa, Y.; Tomishige, K. Metal catalysts for steam reforming of tar derived from the gasification of lignocellulosic biomass. *Bioresour. Technol.* **2015**, *178*, 53–64. [[CrossRef](#)] [[PubMed](#)]
15. Kaewpanha, M.; Guan, G.; Ma, Y.; Hao, X.; Zhang, Z.; Reubroychareon, P.; Kusakabe, K.; Abudula, A. Hydrogen production by steam reforming of biomass tar over biomass char supported molybdenum carbide catalyst. *Int. J. Hydrog. Energy* **2015**, *40*, 7974–7982. [[CrossRef](#)]
16. Sutton, D.; Kelleher, B.; Ross, J.R.H. Review of literature on catalysts for biomass gasification. *Fuel Process. Technol.* **2001**, *73*, 155–173. [[CrossRef](#)]
17. Baker, E.G.; Mudge, L.K.; Brown, M.D. Steam Gasification of Biomass with Nickel Secondary Catalysts. *Ind. Eng. Chem. Res.* **1987**, *26*, 1335–1339. [[CrossRef](#)]
18. Yokoyama, S.; Tomoko, O.; Koguchi, K.; Nakamura, E. Efficient Catalytic Gasification of Cellulose for production of Hydrogen and carbon Monoxide. *Chem. Lett.* **1983**, *12*, 151–154. [[CrossRef](#)]
19. Dayton, D. *A Review of the Literature on Catalytic Biomass Tar Destruction*; National Renewable Energy Laboratory: Lakewood, CO, USA, 2002.
20. Wang, D.; Yuan, W.; Ji, W. Char and char-supported nickel catalysts for secondary syngas cleanup and conditioning. *Appl. Energy* **2011**, *88*, 1656–1663. [[CrossRef](#)]
21. Virginie, M.; Courson, C.; Niznansky, D.; Chaoui, N.; Kiennemann, A. Characterization and reactivity in toluene reforming of a Fe/olivine catalyst designed for gas cleanup in biomass gasification. *Appl. Catal. B Environ.* **2010**, *101*, 90–100. [[CrossRef](#)]
22. Stevens, D.J. *Hot Gas Conditioning: Recent Progress with Larger-Scale Biomass Gasification Systems*; National Renewable Energy Laboratory: Golden, CO, USA, 2001.
23. Shen, Y.; Zhao, P.; Shao, Q.; Takahashi, F.; Yoshikawa, K. *In situ* catalytic conversion of tar using rice husk char/ash supported nickel-iron catalysts for biomass pyrolytic gasification combined with the mixing-simulation in fluidized-bed gasifier. *Appl. Energy* **2014**, *152*, 140–151. [[CrossRef](#)]
24. Shen, Y. Chars as carbonaceous adsorbents/catalysts for tar elimination during biomass pyrolysis or gasification. *Renew. Sustain. Energy Rev.* **2015**, *43*, 281–295. [[CrossRef](#)]
25. Xu, C.C.; Hamilton, S.; Ghosh, M. Hydro-treatment of Athabasca vacuum tower bottoms in supercritical toluene with microporous activated carbons and metal-carbon composite. *Fuel* **2009**, *88*, 2097–2105. [[CrossRef](#)]
26. Van Santen, R.A.; van Leeuwen, P.W.N.M.; Moulijn, J.A.; Averill, B.A. *Catalysis: An Integrated Approach*, 2nd ed.; Elsevier B.V: Amsterdam, The Netherlands, 2000.
27. Serp, B.; Machado, B. *Nanostructured Carbon Materials for Catalysis*; No. 18; Royal Society of Chemistry: London, UK, 2015; Volume 7.
28. Meng, Y.; Young, T.M.; Liu, P.; Contescu, C.I.; Huang, B.; Wang, S. Ultralight carbon aerogel from nanocellulose as a highly selective oil absorption material. *Cellulose* **2015**, *22*, 435–447. [[CrossRef](#)]
29. Pekala, R.W. Organic aerogels from the polycondensation of resorcinol with formaldehyde. *J. Mater. Sci.* **1989**, *24*, 3221–3227. [[CrossRef](#)]
30. Jazaeri, E.; Tsuzuki, T. Effect of pyrolysis conditions on the properties of carbonaceous nanofibers obtained from freeze-dried cellulose nanofibers. *Cellulose* **2013**, *20*, 707–716. [[CrossRef](#)]
31. Guilminot, E.; Fischer, F.; Chatenet, M.; Rigacci, A.; Berthon-fabry, S.; Achard, P.; Chainet, E. Use of cellulose-based carbon aerogels as catalyst support for PEM fuel cell electrodes: Electrochemical characterization. *J. Power Sources* **2007**, *166*, 104–111. [[CrossRef](#)]
32. Jia, X.; Dai, B.; Zhu, Z.; Wang, J.; Qiao, W.; Long, D.; Ling, L. Strong and machinable carbon aerogel monoliths with low thermal conductivity prepared *via* ambient pressure drying. *Carbon N. Y.* **2016**, *108*, 551–560. [[CrossRef](#)]
33. Maldonado-Hódar, F.J.; Moreno-Castilla, C.; Pérez-Cadenas, A.F. Catalytic combustion of toluene on platinum-containing monolithic carbon aerogels. *Appl. Catal. B Environ.* **2004**, *54*, 217–224. [[CrossRef](#)]
34. Moreno-Castilla, C.; Maldonado-Hódar, F.J. Carbon aerogels for catalysis applications: An overview. *Carbon N. Y.* **2005**, *43*, 455–465. [[CrossRef](#)]
35. Aegerter, M.A.; Prassas, M.; Leventis, N.; Koebel, M.M. (Eds.) *Advances in Sol-Gel Derived Materials and Technologies*; Springer: Berlin, Germany, 2012.

36. Qian, D.; Wagner, G.J.; Liu, W.K.; Yu, M.-F.; Ruoff, R.S. Mechanics of carbon nanotubes. *Appl. Mech. Rev.* **2002**, *55*, 495. [[CrossRef](#)]
37. Biener, J.; Stadermann, M.; Suss, M.; Worsley, M.A.; Biener, M.M.; Rose, K.A.; Baumann, T.F. Advanced carbon aerogels for energy applications. *Energy Environ. Sci.* **2011**, *4*, 656. [[CrossRef](#)]
38. Hu, E.; Wu, X.; Shang, S.; Tao, X.; Jiang, S.; Gan, L. Catalytic ozonation of simulated textile dyeing wastewater using mesoporous carbon aerogel supported copper oxide catalyst. *J. Clean. Prod.* **2016**, *112*, 4710–4718. [[CrossRef](#)]
39. Maleki, H. Recent advances in aerogels for environmental remediation applications: A review. *Chem. Eng. J.* **2016**, *300*, 98–118. [[CrossRef](#)]
40. Schrewe, H.W.K. *Fabricación de Aerogel de Carbón Mediante la Carbonización de Celulosa Nanofibrilada y Liofilizada*; University of Concepcion: Concepción, Bío Bío Region, Chile, 2015.
41. George, R.A.; Susott, C.W. *Effects of Ammonium Phosphate and Sulfate on the Pyrolysis and Combustion of Cellulose*; Intermountain Forest and Range Experiment Station: Ogden, UT, USA, 1971.
42. Ishida, O.; Kim, D.Y.; Kuga, S.; Nishiyama, Y.; Brown, R.M. Microfibrillar carbon from native cellulose. *Cellulose* **2004**, *11*, 475–480. [[CrossRef](#)]
43. Tang, M.M.; Bacon, R. Carbonization of Cellulose Fibers—I. Low Temperature Pyrolysis. *Carbon N. Y.* **1964**, *2*, 211–220. [[CrossRef](#)]
44. Brunner, P.H.; Roberts, P.V. The significance of heating rate on char yield and char properties in the pyrolysis of cellulose. *Carbon N. Y.* **1980**, *18*, 217–224. [[CrossRef](#)]
45. Branca, C.; Blasi, C.D. Oxidative devolatilization kinetics of wood impregnated with two ammonium salts. *Fire Saf. J.* **2008**, *43*, 317–324. [[CrossRef](#)]
46. Marsh, H.; Rodriguez-Reinoso, F. *Activated Carbon*, 1st ed.; Elsevier B.V: New York, NY, USA, 2006.
47. Yu, M.; Li, J.; Wang, L. Preparation and characterization of magnetic carbon aerogel from pyrolysis of sodium carboxymethyl cellulose aerogel crosslinked by iron trichloride. *J. Porous Mater.* **2016**, *23*, 997–1003. [[CrossRef](#)]
48. Xie, X.; Goodell, B.; Zhang, D.; Nagle, D.C.; Qian, Y.; Peterson, M.L.; Jellison, J. Characterization of carbons derived from cellulose and lignin and their oxidative behavior. *Bioresour. Technol.* **2009**, *100*, 1797–1802. [[CrossRef](#)] [[PubMed](#)]
49. Grzyb, B.; Hildenbrand, C.; Berthon-Fabry, S.; Bégin, D.; Job, N.; Rigacci, A.; Achard, P. Functionalisation and chemical characterisation of cellulose-derived carbon aerogels. *Carbon N. Y.* **2010**, *48*, 2297–2307. [[CrossRef](#)]
50. Maldonado-Hódar, F.J. Removing aromatic and oxygenated VOCs from polluted air stream using Pt-carbon aerogels: Assessment of their performance as adsorbents and combustion catalysts. *J. Hazard. Mater.* **2011**, *194*, 216–222. [[CrossRef](#)] [[PubMed](#)]
51. Ábrahám, D.; Nagy, B.; Dobos, G.; Madarász, J.; Onyestyák, G.; Trenikhin, M.V.; László, K. Hydroconversion of acetic acid over carbon aerogel supported molybdenum catalyst. *Microporous Mesoporous Mater.* **2014**, *190*, 46–53. [[CrossRef](#)]
52. Park, H.W.; Hong, U.G.; Lee, Y.J.; Song, I.K. Decomposition of 4-phenoxyphenol to aromatics over palladium catalyst supported on activated carbon aerogel. *Appl. Catal. A Gen.* **2011**, *409–410*, 167–173. [[CrossRef](#)]
53. Park, H.W.; Kim, J.K.; Hong, U.G.; Lee, Y.J.; Choi, J.H.; Bang, Y.; Song, I.K. Catalytic decomposition of 1,3-diphenoxybenzene to monomeric cyclic compounds over palladium catalysts supported on acidic activated carbon aerogels. *Appl. Catal. A Gen.* **2013**, *456*, 59–66. [[CrossRef](#)]
54. Rodrigues, C.C.; de Moraes, D.; da Nóbrega, S.W.; Barboza, M.G. Ammonia adsorption in a fixed bed of activated carbon. *Bioresour. Technol.* **2007**, *98*, 886–891. [[CrossRef](#)] [[PubMed](#)]
55. Bandosz, T.J.; Petit, C. On the reactive adsorption of ammonia on activated carbons modified by impregnation with inorganic compounds. *J. Colloid Interface Sci.* **2009**, *338*, 329–345. [[CrossRef](#)] [[PubMed](#)]
56. Duan, X.; Ji, J.; Qian, G.; Fan, C.; Zhu, Y.; Zhou, X.; Chen, D.; Yuan, W. Ammonia decomposition on Fe(1 1 0), Co(1 1 1) and Ni(1 1 1) surfaces: A density functional theory study. *J. Mol. Catal. A Chem.* **2012**, *357*, 81–86. [[CrossRef](#)]
57. Otero, G.S.; Pascucci, B.; Branda, M.M.; Miotto, R.; Belelli, P.G. Evaluating the size of Fe nanoparticles for ammonia adsorption and dehydrogenation. *Comput. Mater. Sci.* **2016**, *124*, 220–227. [[CrossRef](#)]
58. Torrente-Murciano, L.; Hill, A.K.; Bell, T.E. Ammonia decomposition over cobalt/carbon catalysts—Effect of carbon support and electron donating promoter on activity. *Catal. Today* **2017**, *286*, 131–140. [[CrossRef](#)]

59. Smirnova, A.; Wender, T.; Goberman, D.; Hu, Y.L.; Aindow, M.; Rhine, W.; Sammes, N.M. Modification of carbon aerogel supports for PEMFC catalysts. *Int. J. Hydrog. Energy* **2009**, *34*, 8992–8997. [[CrossRef](#)]
60. Wojcieszak, R.; Zieli, M.; Monteverdi, S.; Bettahar, M.M. Study of nickel nanoparticles supported on activated carbon prepared by aqueous hydrazine reduction. *J. Colloid Interface Sci.* **2006**, *299*, 238–248. [[CrossRef](#)] [[PubMed](#)]
61. Xiong, H.; Moyo, M.; Motchelaho, M.A.M.; Jewell, L.L.; Coville, N.J. Fischer-Tropsch synthesis over model iron catalysts supported on carbon spheres: The effect of iron precursor, support pretreatment, catalyst preparation method and promoters. *Appl. Catal. A Gen.* **2010**, *388*, 168–178. [[CrossRef](#)]
62. Asadullah, M. Barriers of commercial power generation using biomass gasification gas: A review. *Renew. Sustain. Energy Rev.* **2014**, *29*, 201–215. [[CrossRef](#)]
63. Bridgwater, A.V.; Boocock, T. *Science in Thermal and Chemical Biomass Conversion*; CPL Press: Newbury, UK, 2006.
64. Poletto, M.; Júnior, H.L.O.; Zattera, A.J. Native cellulose: Structure, characterization and thermal properties. *Materials* **2014**, *7*, 6105–6119. [[CrossRef](#)] [[PubMed](#)]
65. Poletto, M.; Pistor, V.; Zattera, A.J. Structural Characteristics and Thermal Properties of Native Cellulose. In *Cellulose-Fundamental Aspects*; InTech: Caxias do Sul, RS, Brazil, 2013; pp. 45–68.
66. Kim, U.J.; Eom, S.H.; Wada, M. Thermal decomposition of native cellulose: Influence on crystallite size. *Polym. Degrad. Stab.* **2010**, *95*, 778–781. [[CrossRef](#)]
67. Balbuena, P.B.; Gubbins, K.E. Classification of adsorption behavior: Simple fluids in pores of slit-shaped geometry. *Fluid Phase Equilib.* **1992**, *76*, 21–35. [[CrossRef](#)]
68. Choudhary, V.R.; Nayak, V.S.; Choudhary, T.V. Single-component sorption/diffusion of cyclic compounds from their bulk liquid phase in H-ZSM-5 zeolite. *Ind. Eng. Chem. Res.* **1997**, *36*, 1812–1818. [[CrossRef](#)]
69. Arteaga-Pérez, L.E.; Cápiro, O.G.; Delgado, A.M.; Martín, S.A.; Jiménez, R. Elucidating the role of ammonia-based salts on the preparation of cellulose-derived carbon aerogels. *Chem. Eng. Sci.* **2016**, *161*, 80–91. [[CrossRef](#)]
70. Li, Z.Q.; Lu, C.J.; Xia, Z.P.; Zhou, Y.; Luo, Z. X-ray diffraction patterns of graphite and turbostratic carbon. *Carbon N. Y.* **2007**, *45*, 1686–1695. [[CrossRef](#)]
71. Biscoe, J.; Warren, B.E. An X-ray study of carbon black. *J. Appl. Phys.* **1942**, *13*, 364–371. [[CrossRef](#)]
72. Li, X.; Hayashi, J.I.; Li, C.Z. FT-Raman spectroscopic study of the evolution of char structure during the pyrolysis of a Victorian brown coal. *Fuel* **2006**, *85*, 1700–1707. [[CrossRef](#)]
73. Viswanathan, B.; Neel, P.; Varadarajan, T. *Methods of Activation and Specific Applications of Carbon Materials*; National Centre for Catalysis Research Department of Chemistry Indian Institute of Technology Madras: Madras, Chennai, Indian, 2009.
74. Lin, W.-S.; Lin, H.-M.; Chen, H.-H.; Hwu, Y.-K.; Chiou, Y.-J. Shape Effects of Iron Nanowires on Hyperthermia Treatment. *J. Nanomater.* **2013**, *2013*, 9. [[CrossRef](#)]
75. Shen, Y.; Zhao, P.; Shao, Q.; Ma, D.; Takahashi, F. Applied Catalysis B: Environmental. In-situ catalytic conversion of tar using rice husk char-supported nickel-iron catalysts for biomass pyrolysis/gasification. *Appl. Catal. B Environ.* **2014**, *152–153*, 140–151. [[CrossRef](#)]
76. Zheng, W.; Hu, J.; Rappeport, S.; Zheng, Z.; Wang, Z.; Han, Z.; Langer, J.; Economy, J. Activated carbon fiber composites for gas phase ammonia adsorption. *Microporous Mesoporous Mater.* **2016**, *234*, 146–154. [[CrossRef](#)]
77. Keown, D.M.; Li, X.; Hayashi, J.I.; Li, C.Z. Characterization of the structural features of char from the pyrolysis of cane trash using Fourier transform-Raman spectroscopy. *Energy Fuels* **2007**, *21*, 1816–1821. [[CrossRef](#)]
78. Saha, D.; Deng, S. Characteristics of ammonia adsorption on activated alumina. *J. Chem. Eng. Data* **2010**, *55*, 5587–5593. [[CrossRef](#)]
79. Rezaei, E.; Schlageter, B.; Nemati, M.; Predicala, B. Evaluation of metal oxide nanoparticles for adsorption of gas phase ammonia. *J. Environ. Chem. Eng.* **2017**, *5*, 422–431. [[CrossRef](#)]
80. Domingo-García, M.; Groszek, A.J.; López-Garzón, F.J.; Pérez-Mendoza, M. Dynamic adsorption of ammonia on activated carbons measured by flow microcalorimetry. *Appl. Catal. A Gen.* **2002**, *233*, 141–150. [[CrossRef](#)]
81. Vasiliev, L.L.; Kanonchik, L.E.; Kulakov, A.G.; Mishkinis, D.A.; Safonova, A.M.; Luneva, N.K. Activated carbon fiber composites for ammonia, methane and hydrogen adsorption. *Int. J. Low-Carbon Technol.* **2006**, *1*, 95–111. [[CrossRef](#)]

82. Chen, S.; Chen, X.; Zhang, H. Nanoscale size effect of octahedral nickel catalyst towards ammonia decomposition reaction. *Int. J. Hydrog. Energy* **2017**, *42*, 17122–17128. [[CrossRef](#)]
83. Netzer, F.P.; Madey, T.E. Interaction of NH₃ with oxygen-predosed Ni(111). *Surf. Sci.* **1982**, *119*, 422–432. [[CrossRef](#)]
84. Lanzani, G.; Laasonen, K. NH₃ adsorption and dissociation on a nanosized iron cluster. *Int. J. Hydrog. Energy* **2010**, *35*, 6571–6577. [[CrossRef](#)]
85. Diawara, B.; Joubert, L.; Costa, D.; Marcus, P.; Adamo, C. Ammonia on Ni(1 1 1) surface studied by first principles: Bonding, multilayers structure and comparison with experimental IR and XPS data. *Surf. Sci.* **2009**, *603*, 3025–3034. [[CrossRef](#)]
86. Demers, A.L. *Method for the Production of Polymer and Carbon Nanofibers from Lignin and Other Water Soluble Polymers*; The University of Maine: Orono, ME, USA, 2012.
87. ABNT. *8112, Carvão Vegetal-Análise Imediata*; Associação Brasileira de Normas: Rio de Janeiro, Brazil, 1968.
88. De Lange, M.F.; Vlught, T.J.H.; Gascon, J.; Kapteijn, F. Adsorptive characterization of porous solids: Error analysis guides the way. *Microporous Mesoporous Mater.* **2014**, *200*, 199–215. [[CrossRef](#)]
89. Segal, L.; Creely, J.J.; Conrad, M.; Martin, A.E. An Empirical Method for Estimating the Degree of Crystallinity of Native Cellulose Using the X-ray Diffractometer. *Text. Res. J.* **1958**, *29*, 786–794. [[CrossRef](#)]
90. Wada, M.; Okano, T. Localization of I α and I β phases in algal cellulose revealed by acid treatments. *Cellulose* **2001**, *8*, 183–188. [[CrossRef](#)]
91. Gonçalves, M.; Sánchez-García, L.; de Jardim, E.; Silvestre-Albero, J.; Rodríguez-Reinoso, F. Ammonia removal using activated carbons: Effect of the surface chemistry in dry and moist conditions. *Environ. Sci. Technol.* **2011**, *45*, 10605–10610. [[CrossRef](#)] [[PubMed](#)]
92. Kordouli, E.; Kordulis, C.; Lycourghiotis, A.; Cole, R.; Vasudevan, P.T.; Pawelec, B.; Fierro, J.L.G. HDO activity of carbon-supported Rh, Ni and Mo-Ni catalysts. *Mol. Catal.* **2017**, *441*, 209–220. [[CrossRef](#)]
93. Le Leuch, L.M.; Badosz, T.J. The role of water and surface acidity on the reactive adsorption of ammonia on modified activated carbons. *Carbon N. Y.* **2007**, *45*, 568–578. [[CrossRef](#)]
94. Mangun, C.L.; Braatz, R.D.; Economy, J.; Hall, A.J. Fixed Bed Adsorption of Acetone and Ammonia onto Oxidized Activated Carbon Fibers. *Ind. Eng. Chem. Res.* **1999**, *38*, 3499–3504. [[CrossRef](#)]
95. Vannice, M.A. *Kinetics of Catalytic Reactions*; Springer: New York, NY, USA, 2005.



© 2018 by the authors. Licensee MDPI, Basel, Switzerland. This article is an open access article distributed under the terms and conditions of the Creative Commons Attribution (CC BY) license (<http://creativecommons.org/licenses/by/4.0/>).